Acoustic backscatter inversion for suspended sediment concentration and size: A new approach using statistical inverse theory

G. W. Wilson and A. E. Hay

Dalhousie University, 1355 Oxford St., PO Box 15000, Halifax, NS, Canada, B3H 4R2.
greg.wilson@dal.ca, alex.hay@dal.ca

Abstract

A new method is introduced for estimating suspended sediment concentration and grain size from acoustic backscatter observations, incorporating techniques from linearized statistical inverse theory and data assimilation. A series of laboratory experiments with a sediment-laden jet were conducted for the purposes of demonstrating the method. The inversion results show improvements in stability compared to existing methods, in cases with highly-attenuating suspensions. These improvements are due to the use of statistical regularizing assumptions, which act to mitigate issues associated with poor conditioning and nonlinearity in the inverse problem. The new method is also more computationally efficient than existing methods, owing to the use of linearization. Matlab code is provided implementing the new method, see Appendix A.

Keywords: acoustic backscatter, sediment transport, inverse methods

1. Introduction

Acoustic backscatter inversion has been successfully used to characterize the concentration and grain size of sediments suspended in water, in laboratory and field studies (e.g., Hanes et al. (1988); Vincent et al. (1991); Hay and Sheng (1992); Osborne et al. (1994); Hurther et al. (2011); Ruessink et al. (2011); O'Hara Murray et al. (2012); Aagaard (2014); also see reviews by Thorne and Hanes (2002); Thorne and Hurther (2014); and references therein). The principle behind its use involves inversion of a well-established model which describes the average backscattered amplitude from a random field of suspended scatterers. By inverting this model, one can use acoustic backscatter observations to infer the size and concentration of the scatterers. Using this technique, acoustic instruments are capable of collecting sediment measurements at high spatial and temporal resolution, and at far enough range to be considered non-intrusive.

In practice, however, there are several technical barriers to the application of acoustic backscatter inversion. The acoustic scattering properties of natural sediments vary based on their shape and mineralogical composition (e.g., Schaafsma and Hay (1997); Moate and Thorne (2012)), meaning detailed site-specific calibration is required to obtain unbiased results. The instrument itself must also be calibrated (Betteridge et al., 2008; Stanton and Chu, 2008). And other site characteristics such as water temperature, salinity, and sediment size distribution need to be known.

The present work is focused on another, more fundamental, barrier to accurate inversion: suspended sediment backscatter is inherently statistical, i.e. observations are corrupted by statistical uncertainty and/or noise.

This complicates the inversion problem for two reasons. First, the acoustic backscatter model is nonlinear, such that observational noise can lead to large inversion errors when using least-squares-type inversion methods, because of the presence of multiple local minima. This problem is compounded by conditioning issues which occur when the suspension is highly attenuating — that is, when the backscatter at a given range bin depends strongly on the backscatter at previous range bins. In such cases, statistical noise and model errors accumulate along the profile, leading to "blowup" of the inversion. High attenuation occurs when sediment concentration is high, or when high acoustic frequencies are used; high statistical noise occurs with small measurement ensemble sizes. These factors are at odds with measuring at high spatial and temporal resolution in the bottom boundary layer, which is part of the motivation for the present work.

Given the issues just described, inverse algorithms generally need to be stabilized by adding extra constraints, in the form of measurements or assumptions. A promising approach is to incorporate direct measurements of total along-profile attenuation. Thorne et al. (1995) demonstrated the bed echo can be used for this purpose, although this is not possible if the bed echo is signal-saturated (Ruessink et al., 2011). Similarly, Shen and Lemmin (1998) used a system with two facing transducers in order to directly measure and correct for attenuation, however this would seem impractical for non-intrusive profiling applications. Stability can also be improved in cases where the grain size vs. range is known *a priori* (Thorne et al., 2011).

The present work offers a new approach to the stabilization/regularization problem, wherein constraints are added based on statistical assumptions

(section 2). Specifically, the time-dependent sediment concentration and grain size are constrained using *a priori* assumptions regarding (a) the time-averaged state, (b) the magnitude of time-variations, and (c) the statistical variability of the measured data. This information is incorporated using techniques from linearized statistical optimization and data assimilation — for further background on such methods, see, e.g., Aster et al. (2013) for a statistical perspective, or Lewis et al. (2006) for a data assimilation perspective. The statistical method is demonstrated alongside two existing inversion methods, using laboratory observations with a turbulent particle-laden jet (sections 3 and 4). The results show the statistical method to be stable, accurate, and efficient, even in highly-attenuating conditions. An implementation of the method in Matlab code is provided in Appendix A.

2. Methods

2.1. Acoustic Backscatter Model

The theory for acoustic backscatter amplitude from a dilute suspension of particles has been previously described in several studies (e.g., Hay (1983, 1991); Thorne et al. (1991)). A recent review with a focus on inversion was given by Thorne and Hurther (2014); their formulation and notation will be outlined here, and is described in further detail by Thorne and Hardcastle (1997).

Consider a single transducer which insonifies a small volume of suspended particles at range r. The root-mean-square received (backscattered) amplitude, written here as V, can be shown to be

$$V = \frac{K_s K_t}{\psi r} M^{1/2} e^{-2\alpha r}, \tag{1}$$

where

$$K_s = \left(\frac{f_a^2}{\rho_s a}\right)^{1/2}, \quad K_t = \frac{0.96}{k a_t} V_0 r_0 \left[\frac{3c\tau}{16}\right]^{1/2}. \tag{2}$$

In these equations, a is the (effective) particle radius, ρ_s is the particle density, and M is the mass concentration (other variables are described later). In an observational system, acoustic range-gating is used to measure a profile of V in discrete range bins having width Δr. It is assumed the suspension is uniform within each bin, such that the discretized form of the above equations is straightforward: each range bin r_i is associated with a discrete value of a_i and M_i, etc., and integrals are converted to sums.

System calibration factors, which are assumed known, are encapsulated in K_t/ψ. This includes the acoustic wavenumber and phase speed in water, k and c, the pulse duration τ, the effective transducer radius a_t, and a reference value $V_0 r_0$. The factor $0.96/ka_t$ is an approximation (Thorne and Hardcastle, 1997) accounting for integration over the transducer directivity pattern. The factor ψ accounts for near-field spreading effects, as given by Downing et al. (1995),

$$\psi = \frac{1 + 1.35z + (2.5z)^{3.2}}{1.35z + (2.5z)^{3.2}}, \tag{3}$$

where $z = 2r/ka_t^2$.

The intrinsic backscattering properties of the suspension are encapsulated by the terms χ and f_a, which are the normalized total scattering cross section and form factor, respectively, both of which are assumed to depend only on the normalized wavenumber $x = ka$. The form factor appears as part of the factor K_s. The normalized total scattering cross section affects along-path attenuation of the acoustic signal, via the attenuation coefficient $\alpha = \alpha_w + \alpha_s$, in which $\alpha_w(f)$ is attenuation due to water, and α_s is attenuation due to

sediments,

$$\alpha_s = \frac{1}{r}\int_0^r \frac{3\chi}{4a\rho_s} M\, dr. \tag{4}$$

For uniform elastic spherical scatterers, χ and f_a can be exactly specified (Faran, 1951). For natural sediments, variability in particle shape, composition, and size distribution generally necessitate empirical formulations for χ and f_a, which has been the subject of several laboratory studies (Sheng and Hay, 1988; Schaafsma and Hay, 1997; Thorne and Buckingham, 2004; Thorne and Meral, 2008; Moate and Thorne, 2012).

2.2. Direct Inversion

Various methods (Thorne et al. (1991); Hay and Sheng (1992); Crawford and Hay (1993); Lee and Hanes (1995); Thosteson and Hanes (1998); Thorne et al. (2011); among others) have been proposed to invert equation (1), i.e. to determine particle size and concentration profiles based on observations of V at two or more frequencies. These methods seek to determine $M(r)$ and $a(r)$ such that the modeled backscatter (equation (1)) fits the observations as closely as possible, as defined by a specified criterion or cost function. The cost functions that have been considered in existing methods do not attempt to account for statistical errors/noise in the observations or the model; such methods will be referred to here as "direct inversion" methods. A review of such methods was recently given by Thorne and Hurther (2014), who noted that although several methods have been developed, they generally have similar performance.

Two direct inversion methods are considered here, for the purpose of comparison to the statistical method of section 2.3. The first is the method of

Thorne et al. (2011), which was implemented based on Matlab code provided by the authors of Thorne and Hurther (2014) (see internet link in their article). This will be referred to as the "Thorne et al. method". In outline, this method proceeds as follows. For range bin i, a direct search of parameter space is conducted by solving equation (1) for M_i over a user-specified set of candidate values for a_i, separately for each of the observed acoustic frequencies. The contribution of sediment-induced attenuation from bin i itself is incorporated using an iterative scheme. An optimum value of a_i (and hence M_i) is then chosen from the candidate a_i, according to the minimum value of $\langle M - \langle M \rangle \rangle^2 / \langle M \rangle$, where $\langle\rangle$ denotes averaging over the observed acoustic frequencies. The analysis then proceeds to bin $i + 1$.

The second direct inversion method considered here is an adaptation of the "ratio method" originally proposed by Hay and Sheng (1992). For range bin i, the ratio method solves for a_i and then M_i using two separate inversion steps. The first step solves for a_i by considering ratios of backscatter amplitude at different frequencies. In the implementation used here, the value of a_i is chosen by minimizing errors in backscatter ratios over all possible pairs of frequencies, using the following cost function

$$J_a = \sum_{n \neq m} \left[\log \frac{V(f_n)}{V(f_m)} - \log \frac{V^o(f_n)}{V^o(f_m)} \right]^2 , \tag{5}$$

where $V^o(f_n)$ is the observed backscatter amplitude at frequency f_n, and $V(f_n)$ is the corresponding model prediction using equation (1). Once a_i has been determined, the value of M_i is chosen by minimizing

$$J_M = \sum_n \left(\log V(f_n) - \log V^o(f_n) \right)^2 . \tag{6}$$

Similar to the Thorne et al. method, sediment-induced attenuation is incorporated by integrating for α_s over range bins $1, \ldots, i-1$, while the contribution from the i'th bin is incorporated by iteratively applying the method at bin i before proceeding to bin $i+1$.

2.3. Statistical Inversion

2.3.1. Specification of Background State

The statistical inverse method is based on the assumption of linearization about an *a priori* time-averaged, or "background", state, denoted $\log \mathbf{V^b}$, $\log \mathbf{M^b}$, and $\log \mathbf{a^b}$, which is itself estimated based on the time-average of the backscatter observations. It is assumed this time-averaged state can be estimated accurately and stably, based on the fact that statistical uncertainty in the observations will be reduced by time-averaging. Also, because only a single profile is being inverted, manual intervention can be used to detect and fix any non-physical results when estimating the background state. In particular, the inversion can often be constrained using a known parameterized physical model for the time-averaged sediment distribution, as in Lynch et al. (1994).

For the present observations (section 3), the time-average of observations was computed as the root-mean-square of the ensemble-averaged backscatter amplitudes from all 1000 of the 10-ping ensembles (120 seconds data collection, ping interval 12 ms). Even with this level of averaging, the ratio method and the Thorne et al. method both suffered from non-physical discontinuities in the inverted profiles, attributed to nonlinearity in the form function equation (cf. discussion by Thorne and Hardcastle (1997)). To correct this, the time-averaged grain size was further constrained to be spatially uniform

(i.e., a is treated as a scalar parameter), a reasonable first-order model for the present experiment. The ratio method was then applied globally over all range bins to obtain a (cost function equation (5)), and equation (6) was then minimized to obtain M. Sediment-induced attenuation was incorporated in this method by iterative application of the above steps — i.e., α_s was re-calculated for each iteration based on the solution at the previous iteration.

2.3.2. Tangent-Linear Model

Having established the time-averaged background state, we proceed with linearization. Here it will be convenient to work with the logarithm of V, so that equation (1) becomes, in discretized form,

$$\log V = \log \frac{K_t}{\psi r} + \log \frac{f_a}{\rho_s} + \frac{1}{2} \log M - \frac{1}{2} \log a - 2\alpha_w r - 2 \sum_{n=1}^{i} \frac{3\chi}{4a\rho_s} M \Delta r \quad (7)$$

(subscripts denoting the i'th range bin have been suppressed for brevity.) A tangent-linear model is now defined by taking the differential $\delta \log V$ with respect to parameters $\delta \log a$ and $\delta \log M$, linearized around the background state. The equation for $\delta \log V$ is cumbersome, but is straightforward to implement via line-by-line differentiation of the numerical code.

For a profile of observations, $i = 1, \ldots, N_r$, the tangent-linear model can be represented in terms of two (Jacobian) matrices Γ_M and Γ_a, defined by

$$\delta \log \mathbf{V} = \Gamma_M \delta \log \mathbf{M} + \Gamma_a \delta \log \mathbf{a} \quad (8)$$

This can be extended to multiple-frequency observations by considering $\mathbf{V}$ as a concatenation of N_f profiles (i.e., a vector of length $N_r N_f$), in which case Γ_M and Γ_a have dimensions $N_r N_f \times N_r$.

Direct computation of Γ_M and Γ_a can be accomplished by entering identity matrices in place of the vectors $\delta \log \mathbf{M}$ and $\delta \log \mathbf{a}$, respectively, in equation (8). In other words, the tangent-linear model (numerical code) is executed on a unit impulse function for each of the N_r range bins, separately for $\log \mathbf{M}$ and $\log \mathbf{a}$, to obtain each row of Γ_M and Γ_a. While this would seem inefficient, note equation (7) shows that Γ_M and Γ_a consist only of a diagonal part (first five terms of equation (7)), plus a rowwise-constant lower-triangular part representing along-path attenuation (last term in equation (7)). Recognizing this, computing each matrix requires the same order of computational time as evaluating equation (7) over the N_r gridpoints.

2.3.3. Regularized Inversion

Given a vector of backscatter observations, $\log \mathbf{V^o}$, the inversion problem can be stated in linearized form:

$$\log \mathbf{V^o} = \log \mathbf{V^b} + \Gamma_M(\log \mathbf{M} - \log \mathbf{M^b}) + \Gamma_a(\log \mathbf{a} - \log \mathbf{a^b}). \qquad (9)$$

Assuming the problem is not underdetermined (i.e., $N_f \geq 2$), a least-squares matrix inverse solution could be considered. On the other hand, as noted previously, attenuation appears as rowwise-constant lower triangular parts in Γ_M and Γ_a, which, if significant, would tend to cause poor conditioning. In such cases, the inversion would be unstable. An equivalent physical interpretation is that attenuation causes small fluctuations/errors to accumulate along the profile.

Regularizing constraints are now introduced in order to improve the stability of the inverse of equation (9). Define R, the error covariance of the observations, and B_M and B_a, the covariance of the background parame-

ters $\log \mathbf{M^b}$ and $\log \mathbf{a^b}$. The inverse problem is then restated in terms of minimizing the following cost function:

$$\begin{aligned} J &= \left\| \Gamma_M (\log \mathbf{M} - \log \mathbf{M^b}) + \Gamma_a (\log \mathbf{a} - \log \mathbf{a^b}) - \left(\log \mathbf{V^o} - \log \mathbf{V^b} \right) \right\|_R \\ &\quad + \left\| \log \mathbf{M} - \log \mathbf{M^b} \right\|_{B_M} + \left\| \log \mathbf{a} - \log \mathbf{a^b} \right\|_{B_a} . \end{aligned} \tag{10}$$

where the notation $\|\mathbf{x}\|_Y^2 = \mathbf{x}^T Y^{-1} \mathbf{x}$ has been used. The second two (regularizing) terms in equation (10) keep the solution reasonably close to the background state, as quantified by B_M, B_a, and R, and hence dampen the effects of non-physical errors.

The solution for minimizing equation (10) (i.e., the inverted parameters) is

$$\log \mathbf{M}^* = \log \mathbf{M^b} + B_M \Gamma_M^T \left(P + R \right)^{-1} \left(\log \mathbf{V^o} - \log \mathbf{V^b} \right) , \tag{11}$$

and

$$\log \mathbf{a}^* = \log \mathbf{a^b} + B_a \Gamma_a^T \left(P + R \right)^{-1} \left(\log \mathbf{V^o} - \log \mathbf{V^b} \right) , \tag{12}$$

where

$$P = \Gamma_M B_M \Gamma_M^T + \Gamma_a B_a \Gamma_a^T . \tag{13}$$

This linearized solution could potentially be used to form a new background state, in an iterative nonlinear minimization scheme. For the present experiments, such iterations did not yield a significant improvement. This is a possible area for future work.

The choice of B_M and B_a involves *a priori* assumptions, namely the expected magnitude of deviations from the background (time-averaged) state, and the expected spatial correlation (smoothness). Similarly, the observation error covariance R reflects expected variability of $\log \mathbf{V^o}$, e.g. due to random

scattering statistics and instrument noise. The specific covariance models used here are described in section 3.1.

3. Observations

A series of laboratory experiments were conducted in the Dalhousie University jet tank (Hay, 1991; Zedel and Hay, 1999), with the goal of obtaining a baseline data set for testing backscatter inversion with a recently developed multi-frequency acoustic instrument (MFDop; Hay et al. (2012a,b)). The experimental setup is shown in Figure 1. The jet itself is a recirculating system operated by a centrifugal pump. For the present experiments, the average jet centerline velocity was 53–56 cm/s, at the vertical position where all measurements were collected, as measured by a Vectrino II instrument (Zedel and Hay, 2011). Degassed mains fresh water was used, at room temperature 21–22°C.

The experiments used natural beach sand from Queensland Beach, Nova Scotia, which was sieved to extract grain diameters in three ranges: 255–300 μm, 300–355 μm, and 355–400 μm. The primary set of experiments used the 300–355 μm sand, for which six different concentration levels (from 0.5 to 11 g/L) were measured by incrementally adding sand to the jet circuit in between data collections. Four additional experiments were also added to obtain low and medium concentration ($\sim$0.5 and $\sim$7 g/L) measurements for both the 255–300 μm sand and the 355–400 μm sand.

Acoustic backscatter data were collected from the sediment-laden jet using a single-transducer version of the MFDop system, mounted perpendicular to the jet axis of symmetry, at a range 55 cm from the jet centerline, and

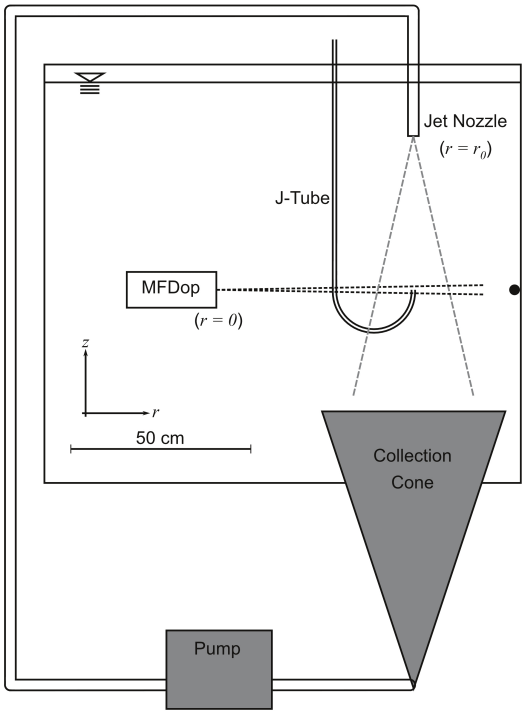

Figure 1: Diagram of experimental apparatus (jet tank). Dashed black lines represent -3 dB acoustic beam half-width ($\sim$1°); dashed gray lines represent the (nominal) full extent of the sediment-laden jet plume. Spherical target is represented as black dot. J-tube was removed from the vicinity of the jet when collecting acoustic data.

Table 1: Acoustic system calibration constant K_t (equation (2)) and -3 dB beam half-width, θ_{-3dB}, at the four acoustic frequencies used in the experiment. Effective transducer radii were measured to be $a_t = 0.011$ m, for all frequencies. Data are calculated using sound speed $c = 1484$ m/s.

f [MHz]	K_t [Vm$^{3/2}$]	θ_{-3dB} [deg]
1.4	0.0065	1.4
1.6	0.0077	1.2
1.8	0.0077	1.1
2.0	0.0060	1.0

43 cm vertically below the jet nozzle (see Figure 1). Measurements were also collected of backscatter from a fixed spherical target mounted on the far side of the jet (at a range of 83 cm), and are used for measuring total sediment-induced attenuation.

The acoustic system transmitted pings of short (5.25 μs) duration, at four acoustic frequencies: 1.4, 1.6, 1.8, and 2.0 MHz. Absolute backscatter calibration of the acoustic system was performed with these same settings, in a separate experiment, using a tungsten carbide standard spherical target and utilizing the short pulse transient-echo technique (Dragonette et al., 1981; Stanton and Chu, 2008). Calibration results are listed in Table 1.

Backscatter amplitudes in the jet were recorded in 4 mm wide range bins, spanning $\pm$10 cm on either side of the jet centerline (nominally the entire jet). Pings were spaced 12 ms apart, such that all acoustic energy was dissipated in the tank between pings. Pulse-to-pulse correlations were low for this sampling scheme (consistent with incoherent scattering statistics as assumed in equation (1)), due in part to rapid (3–4 ping) advection of

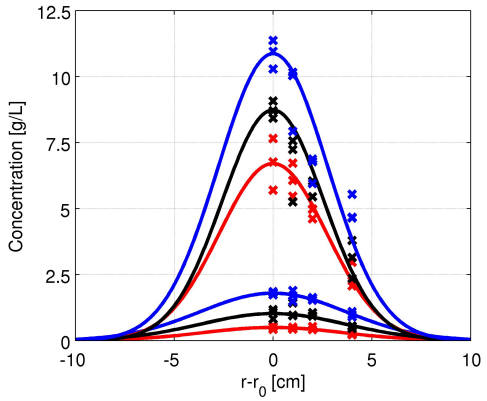

Figure 2: Measured concentration profiles (symbols) and Gaussian fits (lines), for the six experiments with 300–355 μm sand.

sediment through the sampling volume: squared-correlations were less than 0.6 for 95% of all data, with exceptions mainly occurring near the jet edges where the median value was 0.3–0.4. Amplitudes were averaged over 10 pings before being saved to disk, hence the sampling rate for the recorded data is 8.3 Hz. A single collection of MFDop data consisted of 1000 of these 10-ping averages, i.e. 120 seconds.

Immediately after each MFDop data collection, a siphon J-tube was used to collect $\sim$1 L samples of the sediment-laden water at the jet centerline, at the same vertical level as the MFDop. These samples were filtered, dried, and weighed to obtain suspended sediment concentration. Data are summarized in Table 2, which also serves as a summary of all the experiments performed. For the 300–355 μm size class experiments, additional samples were collected at 1, 2, and 4 cm horizontal distance from the jet centerline, to characterize the jet shape. These data are plotted in Figure 2. The measured concentration data are consistent with a Gaussian spatial distribution, with

Table 2: Grain diameter range and jet centerline concentration measurements (three concentration measurements were collected for each experiment).

Expt. ID	Grain Diameter [μm]	Centerline Concentration [g/L]
A	300–355	0.42, 0.52, 0.55
B	300–355	1.2, 1.1, 0.82
C	300–355	1.7, 1.8, 1.9
D	300–355	7.7, 6.8, 5.7
E	300–355	9.1, 8.4, 8.7
F	300–355	11, 10., 11.
G	255–300	0.38, 0.38, 0.35
H	255–300	6.3, 6.2, 6.0
I	355–400	0.62, 0.69, 0.72
J	355–400	6.5, 7.0, 7.3

length scale ∼3 cm. Variability within the triplicate samples is assumed to be due to time-variability of the jet itself, and was observed to increase for the higher concentration experiments. Note the samples were collected in succession at each radial position, and the suction time for each sample was approximately 5 seconds.

3.1. Statistical Parameters

The observation error covariance R was assumed diagonal — that is, observational uncertainty is assumed uncorrelated between different range bins. The primary contribution to observation variance is assumed to be Rayleigh-distributed fluctuations inherent to random scattering (Hay, 1983; Thorne et al., 1993), accounting for the 10-ping averaging in the measurements. An additional variance contribution was added to account for a background noise floor, in the form $V = V_t + \epsilon$, where V_t is the uncontaminated signal, and ϵ is a white noise process. To first order, the noise floor contributes a variance of $\sigma_\epsilon^2/V^2 N_e$ to $\log V$, where σ_ϵ^2 is the variance of ϵ, and $N_e = 10$ is the number of pings being averaged. The present results used $\sigma_\epsilon = 0.5$ mV, based on measurements taken before sand was added to the jet circuit.

The background state covariance matrix B_M was assumed to be of the following simple form:

$$B_M(\Delta i) = \sigma_M^2 e^{-\Delta i^2/2L_i^2}, \tag{14}$$

and similar for B_a. Decorrelation lengths for both parameters were set to $L_i = 2$ range bins (approximately 1 cm). Background state variances for $\log a$ and $\log M$ were specified as $\sigma_a^2 = 0.4^2$ and $\sigma_M^2 = 1^2$, respectively. Results were not strongly sensitive to these parameters, as discussed in section 5.4.

4. Results

4.1. Intrinsic Scattering Properties

Measurements of the normalized total scattering cross section, χ/ρ_s, were obtained by assuming a Gaussian-shaped spatial distribution of suspended sediment (Figure 2),

$$M(r) = M_0 e^{-(r-r_0)^2/2L^2}, \tag{15}$$

expected for round jets sufficiently far downstream of the discharge orifice (Fischer et al., 1979). The total two-way sediment-induced attenuation can then be calculated by comparing the backscatter amplitude at the target behind the jet (Figure 1) to a reference measurement with the jet turned off (still water, no suspended sediment) (Crawford and Hay, 1993), i.e.,

$$\log \frac{V_{\text{on}}}{V_{\text{off}}} = -2r\alpha_s = -\frac{3}{2}\sqrt{2\pi}\frac{LM_0}{a}\chi/\rho_s, \tag{16}$$

which is then solved for χ/ρ_s. This calculation was performed for the experiments with $M_0 > 4$ g/L, and results are shown in Figure 3a. The experimental results showed good agreement with the generic model proposed by Moate and Thorne (2012),

$$\frac{\chi}{\rho_s} = \frac{0.09x^4}{1380 + 560x^2 + 150x^4}, \tag{17}$$

which will therefore be used for inversion.

The normalized form factor, $f_a/\rho_s^{1/2}$, was calculated based on measurements at the jet centerline, where α_s was incorporated using equations (4) and (17). This calculation was performed for the experiments with $M_0 < 4$ g/L, and results are shown in Figure 3b. The generic model proposed by Moate and Thorne (2012) had the same shape as the observed $f_a/\rho_s^{1/2}$, but

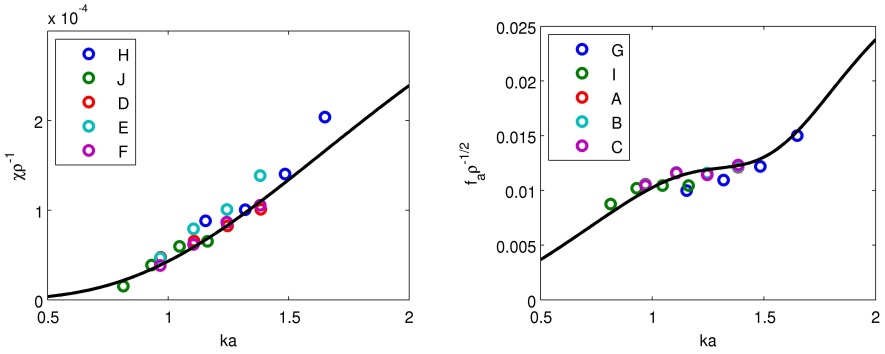

Figure 3: Verification results for normalized form factor and total scattering cross section functions. Symbols represent individual experiments (noted in legend, see Table 2); lines are equations (17) (left panel) and (18) (right panel).

overpredicted the data by an approximately constant factor of 1.4; hence, this factor was simply incorporated into the empirical model,

$$\frac{f_a}{\rho_s^{1/2}} = \frac{\left(1 - 0.25e^{-(x-1.5)^2/0.35^2}\right)\left(1 + 0.6e^{-(x-2.9)^2/1.15^2}\right)x^2}{1.4(42 + 28x^2)}. \qquad (18)$$

4.2. Inversion Results

Figures 4–7 show inverted time-dependent sediment concentration and grain diameter, comparing the statistical inverse method to the two direct inverse methods. Results are shown for the lowest and highest concentration experiments with 300–355 μm sand, i.e. $\sim$0.5 g/L (experiment A, Figures 4 and 5), and $\sim$11 g/L (experiment F, Figures 6 and 7), respectively. These results are representative of the overall results for the full series of experiments.

Time averages of inversion results are shown in Figures 8 and 9. Instability in the direct inversion result leads to an overall bias at high attenuation, whereas the statistical inversion result is centered on its imposed

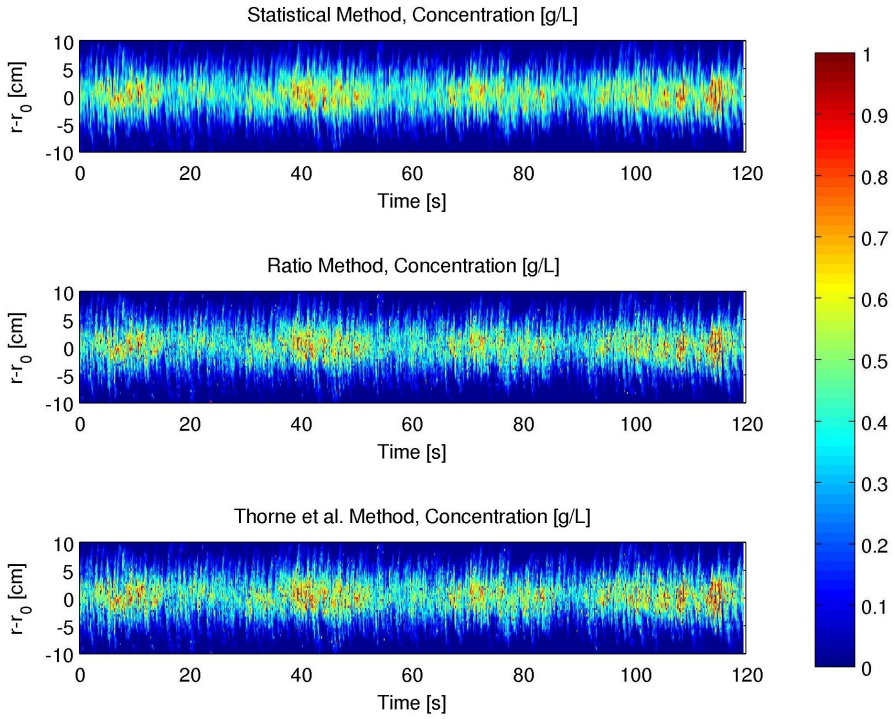

Figure 4: Time series of suspended sediment concentration inversion results at low concentration, experiment A.

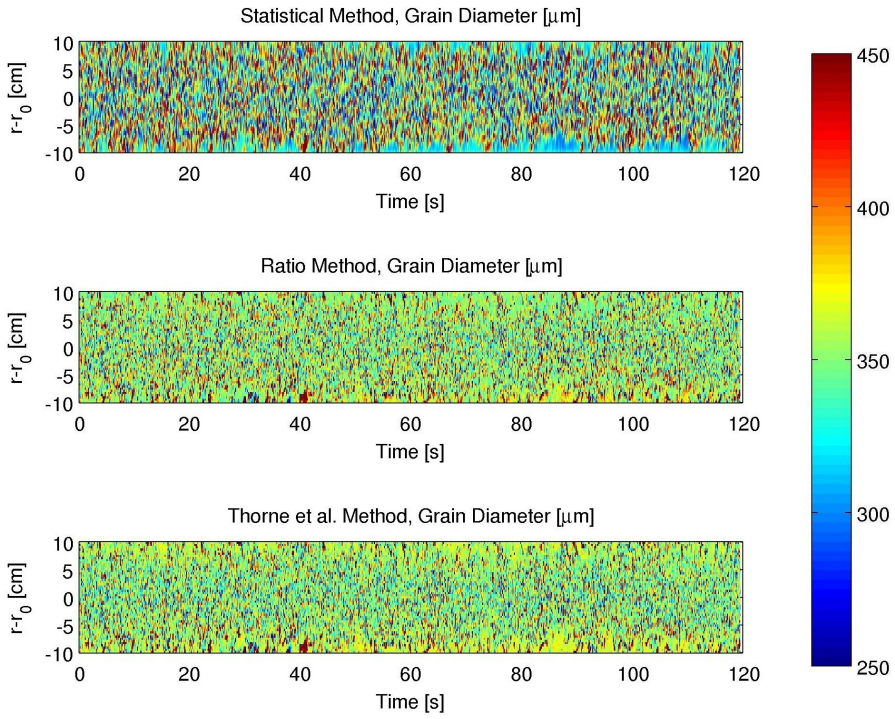

Figure 5: Time series of sediment grain diameter inversion results at low concentration, experiment A.

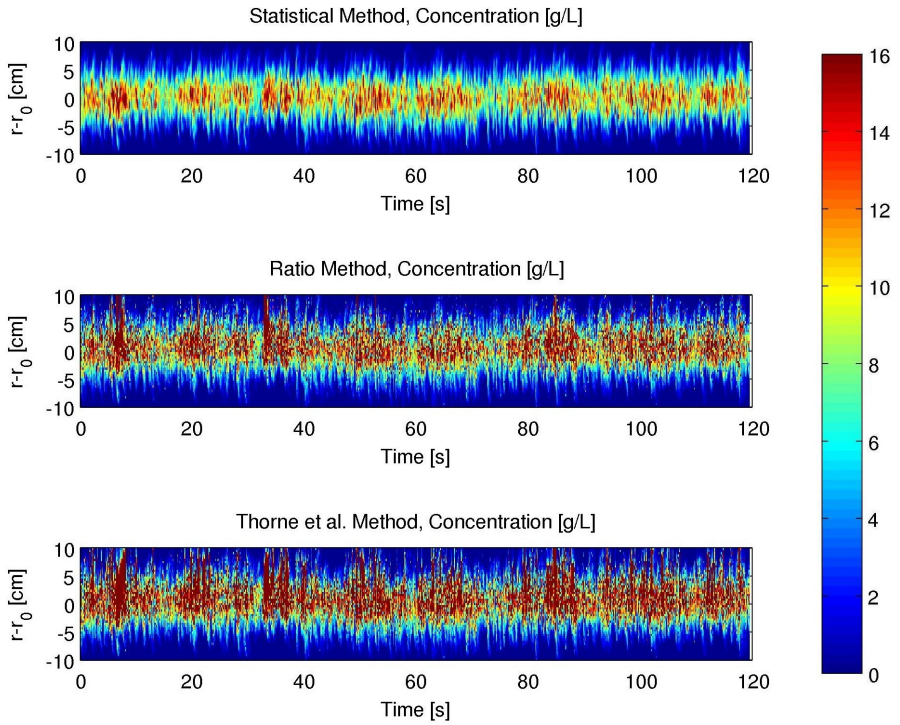

Figure 6: Time series of suspended sediment concentration inversion results at high concentration, experiment F.

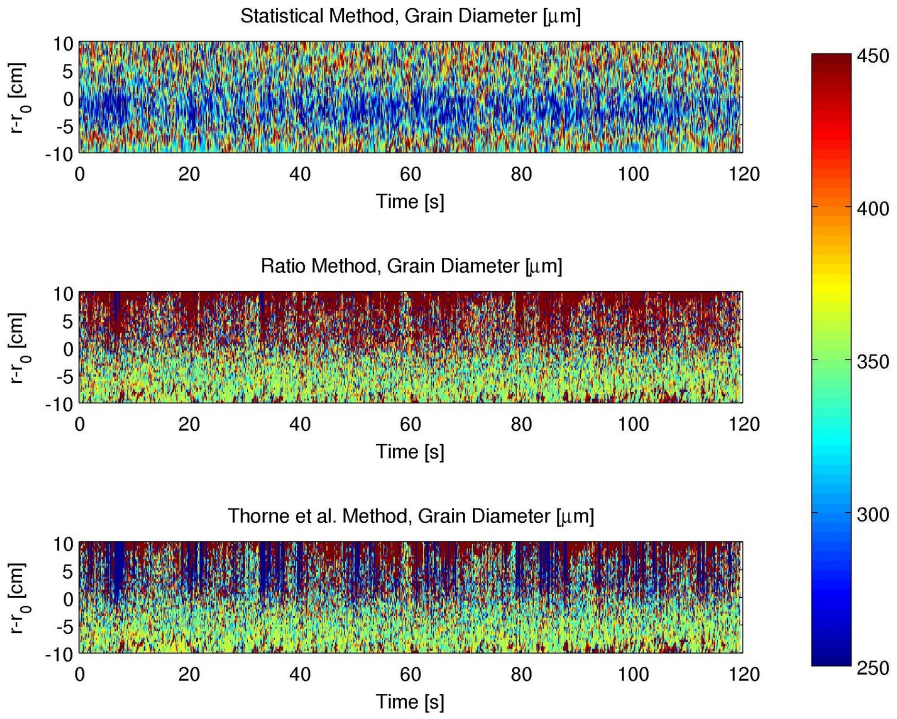

Figure 7: Time series of suspended sediment grain diameter inversion results at high concentration, experiment F.

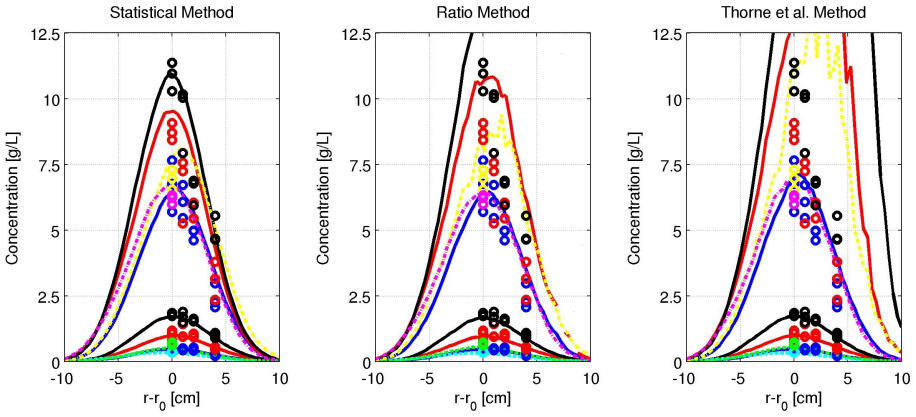

Figure 8: Time averages of suspended sediment concentration inversion results. Solid lines: 300–355 μm sand (experiments A-F); cyan and magenta dashed lines: 255–300 μm sand (experiments G-H); green and yellow dashed lines: 355–425 μm sand (experiments I-J); symbols: suction sample measurements, cf. Figure 2.

time-averaged state. To reduce the effect of outliers (spikes) in the direct inversion results in these figures, despiking was applied before computing time averages: data were discarded if either the inverted M or a deviated from their time-averaged value by more than four standard deviations.

Time-averaged inverted concentration and grain diameter are compared to measurements in Tables 3 and 4. As previously, despiking was applied before computing time averages of the inversion results. In the table, the measured centerline concentration is represented by the average of triplicate J-tube concentration measurements, and grain diameter is represented by the average of the bracketing sieve diameters used for preparing the sediment samples.

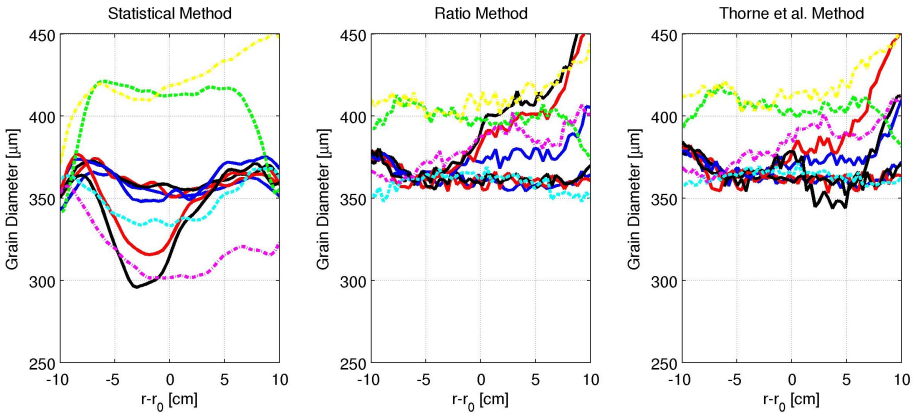

Figure 9: Time averages of sediment grain diameter inversion results, with line colors matching Figure 8.

Table 3: Jet centerline inverted time-averaged concentration results, compared to measurements. All data are reported in g/L units.

Expt. ID	Average Measured	Statistical Method	Ratio Method	Thorne et al. Method
A	0.5	0.48	0.46	0.48
B	1.0	0.99	0.96	0.99
C	1.8	1.7	1.7	1.7
D	6.7	6.5	6.4	7.0
E	8.7	9.5	11	13
F	11	11	14	23
G	0.37	0.33	0.31	0.32
H	6.2	6.7	6.4	6.9
I	0.68	0.51	0.54	0.54
J	6.9	7.7	8.1	11

Table 4: Jet centerline inverted time-averaged grain diameter results, compared to measurements. All data are reported in μm units.

Expt. ID	Average Measured	Statistical Method	Ratio Method	Thorne et al. Method
A	330	350	360	360
B	330	350	360	360
C	330	360	360	360
D	330	350	370	370
E	330	320	380	380
F	330	320	390	380
G	280	330	360	360
H	280	300	390	390
I	390	410	400	400
J	390	420	410	410

5. Discussion

5.1. Concentration Results

At low concentrations (experiments A–C, G, and I, which had centerline concentrations less than ∼7 g/L), all three methods produced very similar inverted concentrations, and were in good overall agreement with measurements (see Table 3). The time-dependent concentrations obtained from the direct inversion methods (e.g., Figure 4) were somewhat less smooth than those of the statistical method, as would be expected given the imposed smoothing in the statistical method. Direct inverse results also included some non-physical spikes, which could be detected and removed.

At higher concentrations (experiments D–F, H and J, which had centerline concentrations greater than ∼7 g/L), the direct inverse methods exhibited instability, e.g. Figures 6 and 7. Stability problems were generally initiated at points with large concentration (i.e., near the jet centerline, and at times when the jet concentration became slightly elevated), and then propagated to longer ranges. The threshold for instability can be judged using Experiment D, which included only a few isolated blowups. Based on the observed concentration and grain diameter, this experiment had a maximum attenuation coefficient of $r\alpha_s = 0.23$.

When present, instability is associated with discontinuities in grain size, and corresponding discontinuities in concentration. The most severe discontinuities are generally caused by jumps between different local minima in the cost function; that is, observation error/noise can cause a local minimum to incorrectly become the global minimum. The additional regularizing terms in the statistical method suppress this behaviour; overall errors/bias were

still larger than for low concentration cases (e.g., grain size is consistently underpredicted near the center of the jet in Figure 7), but this did not lead to uncontrolled blowup as in the direct methods.

5.2. Grain Size Results

None of the methods produced smooth time-dependent grain size results (e.g., Figures 5 and 7), for any of the experiments, although the time-averaged grain size results (Figure 9 and Table 4) were relatively smooth and repeatable over different experiments and between different methods. Time-averaged inverted grain sizes were generally overpredicted when compared to the sieved grain size, see Table 4, although the relatively larger/smaller grain sizes used in experiments G-J were to some extent detected.

The reason for the apparent noise in inverted grain size is unknown, but may reflect time-variability in the intrinsic scattering properties, χ and f_a, which are not included in the present scattering model but can be caused by random fluctuations in particle shape, composition, and orientation. The inverted grain size variability could be reduced to a reasonable level (as compared to the sieved range) if the acoustic backscatter data were subjected to a moving time-average with a window of order 1–2 seconds. In principle a similar result could be obtained by extending the background covariance matrices B_M and B_a into the time domain, but this has not yet been implemented. The inversion noise was also reduced if the value of σ_a was reduced to be closer to to the known (sieved) grain size range, but this would not be justified in more general experimental settings where the size range is generally not well-known.

5.3. Sensitivity to Scattering Model

A potential source of error in the inversion results is due to mis-calibration of the semi-empirical models for normalized total scattering cross section and form factor (equations (17) and (18)). Following Thorne et al. (2011), variations on these models were considered of the form

$$f_a' = \mathcal{B} f_a, \quad \chi' = \mathcal{B}\chi, \tag{19}$$

where

$$\mathcal{B} = \beta \frac{\beta x^2 + 1}{x^2 + 1}. \tag{20}$$

The factor β is treated as a tuning parameter — measurements shown in Figure 3 suggest $\beta = 1 \pm 0.1$. To investigate the sensitivity to this potential source of error, the experiments of section 4.2 were repeated using $\beta = 0.9$ and $\beta = 1.1$.

For $\beta = 1.1$, the direct inverse methods remained unstable for high concentrations, whereas the statistical method remained stable, similar to the $\beta = 1$ results. For $\beta = 0.9$, the direct inverse methods were less unstable, although divergence still occurred for the highest concentration experiments; again, the statistical method remained stable.

In all cases for which the inversions were stable, concentration was consistently overpredicted using $\beta = 0.9$, and underpredicted using $\beta = 1.1$, whereas results using $\beta = 1$ did not have consistent bias. The average inverted centerline concentration for experiment A, for example, was 0.67 g/L when using $\beta = 0.9$, and 0.35 g/L when using $\beta = 1.1$ (for the statistical method; other methods gave similar results). Hence, further tuning of β is not expected to result in significantly more accurate inversion results for

the present data. This indicates that the instability observed in the direct inverse results was mainly associated with high concentrations, and was not an effect of model (mis-)calibration.

5.4. Sensitivity to Parameters

The detailed results of the statistical inverse method are dependent on the selection of parameters σ_M, σ_a, and L_i (equation (14)). To investigate sensitivity to these parameters, additional inversions were performed as in section 4.2, but using $\sigma_a = 0.8$ and $\sigma_M = 2$ (i.e., twice their original values). Results differed by an average of 3–9% in concentration, and 2–5% in grain size. Similarly, doubling L_i (from 2 to 4 gridpoints) resulted in smoother inverse results, as would be expected, with average differences of 10–19% in concentration, and 4–7% in grain size. None of the above tests resulted in qualitative changes in the inverted concentration or grain size. In that sense, the results of the statistical method are robust with respect to reasonable changes/errors in the background covariance parameters.

5.5. Computational Efficiency

The linearized framework used here, while approximate, has an advantage of being computationally efficient. The bulk of the computation involves estimating the background time-averaged state, and the corresponding tangent-linear matrices, each of which requires the same order of computational time as direct inversion of a single profile. Once that information is stored, equations (11) and (12) are easily solved for the time-dependent profiles. By contrast, the direct inverse methods require repeated evaluations of equation (1) to locate the minimum of a nonlinear cost function at each profile.

For the ratio method, this was implemented using a bounded golden-section search (Matlab's fminbnd); the Thorne et al. method used a direct search in the range $a = 50 - 300$ μm, in increments of 1 μm. For the present data set, the statistical method ran approximately 40 times faster than the Thorne et al. method, and approximately 140 times faster than the ratio method.

6. Conclusions

A new statistical method has been introduced for inversion of multi-frequency acoustic backscatter data to obtain suspended particle size and concentration. The new method targets known stability issues with backscatter inversion (e.g., see Thorne et al. (2011), and references therein), which tend to arise when inverting backscatter data over short averaging times (i.e., high statistical noise) and at high concentrations (i.e., high sediment-induced attenuation). In such cases, extra constraints must be added to obtain stability. In the statistical method, the additional constraints are based on an *a priori* estimated time-averaged state, the assumed variability about that state, and the statistical properties of the observations. These constraints are incorporated using standard techniques from linearized inverse theory and data assimilation (Lewis et al., 2006; Aster et al., 2013).

The method was demonstrated using high spatial/temporal resolution laboratory experiments with a sediment-laden jet. Results were compared to two "direct inverse" (i.e., non-statistical) methods: the ratio method (Hay and Sheng, 1992), and the method of Thorne et al. (2011). All three methods produced very similar results in conditions where sediment-induced acoustic attenuation was weak, i.e. low-concentration conditions. For high-

concentration conditions (greater than $\sim$7 g/L), the direct inverse methods exhibited instability, resulting in inaccurate inverse results, whereas the statistical method remained stable. The statistical method is also more computationally efficient than direct methods for inverting the present data, owing to the use/assumption of linearized dynamics.

Acknowledgements

The authors wish to thank Richard Cheel, Walter Judge, Jenna Hare, and Winson Li for their assistance with the laboratory experiments. We also thank P. Thorne and D. Hurther, for making their inversion code available. This work was supported by the Atlantic Innovation Fund, the National Sciences and Engineering Research Council of Canada, and Nortek.

Appendix A. Matlab Code for Statistical Acoustic Backscatter Inversion

Matlab code implementing the inversion method is provided at *, or by contacting the authors. The code consists of a forward model for calculating acoustic backscatter from a given suspended sediment field (following Thorne and Hurther (2014); section 2.1), a differentiated (tangent-linear, Jacobian) version of this forward model (section 2.3.2), and an implementation of the linearized statistical inversion scheme (section 2.3). This code is intended for academic use only, and no support is provided.

Aagaard, T., 2014. Sediment supply to beaches: Cross-shore sand transport on the lower shoreface. Journal of Geophysical Research 119 (4), 913–926.

Aster, R. C., Borchers, B., Thurber, C. H., 2013. Parameter estimation and inverse problems. Academic Press.

Betteridge, K. F., Thorne, P. D., Cooke, R. D., 2008. Calibrating multi-frequency acoustic backscatter systems for studying near-bed suspended sediment transport processes. Continental Shelf Research 28 (2), 227–235.

Crawford, A., Hay, A. E., 1993. Determining suspended sand size and concentration from multifrequency acoustic backscatter. Journal of the Acoustical Society of America 94 (6), 3312–3324.

Downing, A., Thorne, P. D., Vincent, C. E., 1995. Backscattering from a suspension in the near field of a piston transducer. Journal of the Acoustical Society of America 97 (3), 1614–1620.

Dragonette, L. R., Numrich, S., Frank, L. J., 1981. Calibration technique for acoustic scattering measurements. Journal of the Acoustical Society of America 69 (4), 1186–1189.

Faran, J. J., 1951. Sound scattering by solid cylinders and spheres. Journal of the Acoustical Society of America 23 (4), 405–418.

Fischer, B., List, E., Koh, R., Imberger, J., Brooks, N., 1979. Mixing in Coastal and Inland Waters. Academic, New York, 483 pp.

Hanes, D., Vincent, C., Huntley, D., Clarke, T., 1988. Acoustic measurements of suspended sand concentration in the C2S2 experiment at Stanhope Lane, Prince Edward Island. Marine Geology 81 (1), 185–196.

Hay, A. E., 1983. On the remote acoustic detection of suspended sediment at long wavelengths. Journal of Geophysical Research 88 (C12), 7525–7542.

Hay, A. E., 1991. Sound scattering from a particle-laden, turbulent jet. Journal of the Acoustical Society of America 90 (4), 2055–2074.

Hay, A. E., Sheng, J., 1992. Vertical profiles of suspended sand concentration and size from multifrequency acoustic backscatter. Journal of Geophysical Research 97 (C10), 15661–15677.

Hay, A. E., Zedel, L., Cheel, R., Dillon, J., 2012a. Observations of the vertical structure of turbulent oscillatory boundary layers above fixed roughness beds using a prototype wideband coherent Doppler profiler: 1. The oscillatory component of the flow. Journal of Geophysical Research 117(C03005).

Hay, A. E., Zedel, L., Cheel, R., Dillon, J., 2012b. Observations of the vertical structure of turbulent oscillatory boundary layers above fixed roughness using a prototype wideband coherent Doppler profiler: 2. Turbulence and stress. Journal of Geophysical Research 117(C03006).

Hurther, D., Thorne, P. D., Bricault, M., Lemmin, U., Barnoud, J.-M., 2011. A multi-frequency acoustic concentration and velocity profiler (ACVP) for boundary layer measurements of fine-scale flow and sediment transport processes. Coastal Engineering 58 (7), 594–605.

Lee, T. H., Hanes, D. M., 1995. Direct inversion method to measure the concentration profile of suspended particles using backscattered sound. Journal of Geophysical Research 100 (C2), 2649–2657.

Lewis, J. M., Lakshmivarahan, S., Dhall, S., 2006. Dynamic data assimilation: a least squares approach. Cambridge University Press.

Lynch, J. F., Irish, J. D., Sherwood, C. R., Agrawal, Y. C., 1994. Determining suspended sediment particle size information from acoustical and optical backscatter measurements. Continental Shelf Research 14 (10), 1139–1165.

Moate, B. D., Thorne, P. D., 2012. Interpreting acoustic backscatter from suspended sediments of different and mixed mineralogical composition. Continental Shelf Research 46, 67–82.

O'Hara Murray, R. B., Hodgson, D. M., Thorne, P. D., 2012. Wave groups and sediment resuspension processes over evolving sandy bedforms. Continental Shelf Research 46, 16–30.

Osborne, P. D., Vincent, C. E., Greenwood, B., 1994. Measurement of suspended sand concentrations in the nearshore: field intercomparison of optical and acoustic backscatter sensors. Continental Shelf Research 14 (2), 159–174.

Ruessink, B. G., Michallet, H., Abreu, T., Sancho, F., Van der Werf, J., Silva, P., et al., 2011. Observations of velocities, sand concentrations, and fluxes under velocity-asymmetric oscillatory flows. Journal of Geophysical Research 116 (C3).

Schaafsma, A. S., Hay, A. E., 1997. Attenuation in suspensions of irregularly shaped sediment particles: A two-parameter equivalent spherical scatterer model. Journal of the Acoustical Society of America 102 (3), 1485–1502.

Shen, C., Lemmin, U., 1998. Improvements in acoustic sediment concentration profiling using an LMS compensation algorithm. Oceanic Engineering, IEEE Journal of 23 (2), 96–104.

Sheng, J., Hay, A. E., 1988. An examination of the spherical scatterer approximation in aqueous suspensions of sand. Journal of the Acoustical Society of America 83 (2), 598–610.

Stanton, T. K., Chu, D., 2008. Calibration of broadband active acoustic systems using a single standard spherical target. Journal of the Acoustical Society of America 124 (1), 128–136.

Thorne, P., Vincent, C., Hardcastle, P., Rehman, S., Pearson, N., 1991. Measuring suspended sediment concentrations using acoustic backscatter devices. Marine Geology 98 (1), 7–16.

Thorne, P. D., Buckingham, M. J., 2004. Measurements of scattering by suspensions of irregularly shaped sand particles and comparison with a single parameter modified sphere model. Journal of the Acoustical Society of America 116 (5), 2876–2889.

Thorne, P. D., Hanes, D. M., 2002. A review of acoustic measurement of small-scale sediment processes. Continental Shelf Research 22 (4), 603–632.

Thorne, P. D., Hardcastle, P. J., 1997. Acoustic measurements of suspended sediments in turbulent currents and comparison with in-situ samples. Journal of the Acoustical Society of America 101 (5), 2603–2614.

Thorne, P. D., Hardcastle, P. J., Soulsby, R. L., 1993. Analysis of acoustic measurements of suspended sediments. Journal of Geophysical Research 98 (C1), 899–910.

Thorne, P. D., Holdaway, G. P., Hardcastle, P. J., 1995. Constraining acoustic backscatter estimates of suspended sediment concentration profiles using the bed echo. Journal of the Acoustical Society of America 98 (4), 2280–2288.

Thorne, P. D., Hurther, D., 2014. An overview on the use of backscattered sound for measuring suspended particle size and concentration profiles in non-cohesive inorganic sediment transport studies. Continental Shelf Research 73, 97–118.

Thorne, P. D., Hurther, D., Moate, B. D., 2011. Acoustic inversions for measuring boundary layer suspended sediment processes. Journal of the Acoustical Society of America 130 (3), 1188–1200.

Thorne, P. D., Meral, R., 2008. Formulations for the scattering properties of suspended sandy sediments for use in the application of acoustics to sediment transport processes. Continental Shelf Research 28 (2), 309–317.

Thosteson, E. D., Hanes, D. M., 1998. A simplified method for determining sediment size and concentration from multiple frequency acoustic backscatter measurements. Journal of the Acoustical Society of America 104 (2), 820–830.

Vincent, C. E., Hanes, D. M., Bowen, A. J., 1991. Acoustic measurements of

suspended sand on the shoreface and the control of concentration by bed roughness. Marine Geology 96 (1), 1–18.

Zedel, L., Hay, A., 2011. Turbulence measurements in a jet: Comparing the Vectrino and Vectrino II. In: Current, Waves and Turbulence Measurements (CWTM), 2011 IEEE/OES 10th. IEEE, pp. 173–178.

Zedel, L., Hay, A. E., 1999. A coherent Doppler profiler for high-resolution particle velocimetry in the ocean: Laboratory measurements of turbulence and particle flux. Journal of Atmospheric and Oceanic Technology 16 (8), 1102–1117.